

Article

Acceleration of Persulfate Activation by MIL-101(Fe) with Vacuum Thermal Activation: Effect of FeII/FeIII Mixed-Valence Center

Jieyang Yang, Zequan Zeng *, Zhanggen Huang * and Yan Cui

State Key Laboratory of Coal Conversion, Institute of Coal Chemistry, Chinese Academy of Sciences, Taiyuan 030001, China; yangjy@sxicc.ac.cn (J.Y.); cuiyan@sxicc.ac.cn (Y.C.)

* Correspondence: zengzequan@sxicc.ac.cn (Z.Z.); zghuang@sxicc.ac.cn (Z.H.); Tel.: +86-351-4043727 (Z.H.); +86-351-4048310 (Z.Z.)

Received: 29 September 2019; Accepted: 26 October 2019; Published: 29 October 2019



Abstract: In this work, the activation effect of vacuum thermal treatment on MIL-101(Fe) (MIL: Materials of Institute Lavoisier) was investigated for the first time. It demonstrated that vacuum thermal activation could accelerate the activation of persulfate (PS) by MIL-101(Fe), and the enhancement of the catalytic capacity of MIL-101(Fe) was mainly attributed to the change in the FeII/FeIII mixed-valence center. The results of the SEM and XRD showed that vacuum thermal activation had a negligible effect on the crystal structure and particle morphology of MIL-101(Fe). Meanwhile, the higher temperature of vacuum thermal activation caused a higher relative content ratio of FeII/FeIII. A widely used azo dye, X-3B, was chosen as the probe molecule to investigate the catalytic performance of all samples. The results showed that the activated samples could remove X-3B more effectively, and the sample activated at 150 °C without regeneration could effectively activate PS to remove X-3B for at least 5 runs and approximately 900 min. This work highlights the often-overlooked activation effect of vacuum thermal treatment and provides a simple way to improve the catalytic capacity and reusability of MIL-101(Fe) which is beneficial for the application of MIL-101(Fe)/PS systems in azo dye wastewater treatment.

Keywords: vacuum thermal activation; MIL-101(Fe); persulfate; azo dye

1. Introduction

Effluents of textile industries, pulp mills, and dyestuff manufacturing are known to contain considerable colors which are caused by dyes. Among these dyes, azo dyes constitute the largest and the most important class of commercial dyes [1,2]. Numerous studies on dyes have shown that azo dyes are unlikely to be biodegradable, toxic, and possibly carcinogenic and mutagenic to living organisms [3–5]. Thus, efficient removal of azo dyes is necessary and important.

Advanced oxidation processes (AOPs) have proved to be economical and efficient in treating dye effluents and producing high-quality water [6,7]. Sulfate radical-based AOPs have been regarded as effective technologies for degradation of recalcitrant organic contaminants and received considerable attention for destruction of azo dye compounds [8–10]. In general, persulfate (PS) exhibits low reactivity toward contaminants in water. Therefore, a proper activation method for PS is crucial and requisite in wastewater treatment. The most extensively used activators for PS are transition metals, including Co, Ag, Fe, etc. [11–14]. Among these transition metals, Fe has often been selected as a PS activator owing to its low toxicity, low cost, high activity, and natural abundance [15]. However, the Fe/PS system has some intrinsic drawbacks, such as strict pH range limits and accumulation of ferric oxide sludge, which limit its widespread application [16–18].

Thus, researchers have focused on preparing Fe-containing heterogeneous catalysts with various support materials to solve the problems mentioned above [19–22]. Metal–organic frameworks (MOFs) are a class of versatile inorganic–organic hybrid materials which are composed of metal atoms or clusters linked by polydentate organic ligands [23]. Iron-based MOFs are extremely attractive, since they have a high content of active metal sites and iron-containing complexes are commonly used in catalysis [24,25]. The MIL (Materials of Institute Lavoisier) family, built from trivalent metal centers and carboxylate-bridging ligands pioneered by Férey and co-workers [26], has good stability in water. Thus, we focused on the Fe-based MILs and some of them have been reported to activate $\text{H}_2\text{O}_2/\text{PS}$ for organic contaminants removal. For instance, MIL-53(Fe) was proved to accelerate removal of acid orange 7 with PS and visible light [27]. The MIL-88A, produced at the synthesis temperature of 85 °C, had good catalytic performance for orange G removal through PS activation [28]. Furthermore, Li and Guo et al. [29] conducted a comparison between MIL-101(Fe), MIL-100(Fe), MIL-53(Fe), and MIL-88B(Fe) for acid orange 7 removal via PS activation, while MIL-101(Fe) had the best performance on adsorption and catalytic oxidation.

As mentioned above, MIL-101(Fe) is a promising candidate for PS activation. However, the catalytic performance of bare MIL-101(Fe) was not satisfactory due to the fact of it possessing a high proportion of FeIII sites in the active metal center [30]. Some studies focused on modification with an Fe^{2+} -containing compound. For example, Wang et al. [31,32] prepared a ferrocene-modified MIL-101(Fe) which exhibits excellent Fenton-like activity through the electron transfer of ferrocene as a redox mediator. Meanwhile, some efforts have been devoted to the synthesis of a composite catalyst with MIL-101(Fe). A core–shell $\text{Fe}_3\text{O}_4/\text{MIL-101}$ composite was successfully synthesized by Yue et al. [30] which was introduced as a catalyst to generate powerful radicals from PS for the removal of acid orange 7. A composite consisting of graphitic carbon nitride and MIL-101(Fe) was reported by Gone et al. [33] which exhibited improved photocatalytic performance for bisphenol A degradation in the presence of PS.

However, considering the advantages of MIL-101(Fe) itself, such as a high content of Fe, a high dispersibility of active metal sites, and a crystalline open structure which provides efficient entrances for penetration of reactant molecules, a suitable method to activate MIL-101(Fe) may be a more efficient and simple way to improve its catalytic capacity for PS activation. According to Wuttke's study [34], heating to 423 K under a helium flow could cause a huge departure of free water molecules in frameworks of MIL-100(Fe). Meanwhile, Aggarwal et al. [35] found that a long-time vacuum thermal treatment (120 °C, 24 h) would lead to a change in the interpenetration and a transformation of the crystalline phase on Zn-based MOF. In addition, Yoon et al. [36] found that thermal activation at inert gas flow or in vacuum can introduce reducibility to MIL-100(Fe), and the treatment leads to a dramatic improvement of preferential gas sorption due to the formation of FeII sites.

As a drying method, vacuum thermal treatment is widely used in material preparation. However, the potential activation effect of vacuum thermal treatment was often ignored by researchers. Based on the limited relevant studies mentioned above, we speculated that the vacuum thermal activation could also remove free water molecules in the framework and, hence, provide more feasible active sites for PS activation. Meanwhile, vacuum thermal activation may lead to a change in the FeII/FeIII mixed-valence center which may affect the catalytic capacity of MIL-101(Fe) for PS activation.

Therefore, in this work, MIL-101(Fe) was prepared and treated in vacuum at different temperatures. Then, the samples were characterized and used for PS activation to remove a widely used azo dye, X-3B. The objective of this study was to investigate the change of catalytic performance of MIL-101(Fe) after the vacuum thermal activation and try to understand the role of the FeII/FeIII mixed-valence center in MIL-101(Fe) for PS activation. Meanwhile, the stability and reusability of activated MIL-101(Fe) were also evaluated through long-term PS activation (5 cycles).

2. Results and Discussion

2.1. Characterization

The MIL-101(Fe) was synthesized and divided into five parts. One was denoted as M-0 without further treatment, and the other four were treated, respectively, in vacuum at a required temperature (120 °C, 150 °C, 170 °C and 200 °C) for 7 h and denoted as M-120, M-150, M-170, and M-200, respectively. The X-ray diffraction (XRD) patterns of all samples are shown in Figure 1. The main diffraction peaks of M-0 are in accordance with the data reported in the literature [37–39], indicating that the MIL-101(Fe) was successfully prepared. Meanwhile, the XRD patterns of activated samples were very similar to that of as-prepared MIL-101(Fe), and no additional signals are observed. This confirmed that the vacuum thermal activation did not change the crystalline structure of MIL-101(Fe). Moreover, the high intensities of the peaks suggested a high degree of crystallinity for all samples.

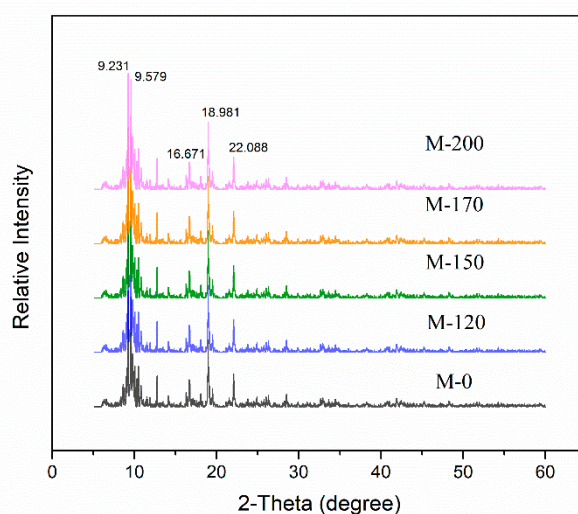


Figure 1. XRD patterns of as-prepared MIL-101(Fe) and activated samples.

A scanning electron microscope (SEM) was used to characterize the surface morphology of prepared samples. As shown in Figure 2A, the sample M-0 had the characteristic of a typical cubo-octahedral shape which was previously reported for MIL-101(Fe) [40]. It can also be seen from Figure 2A(1) that the MIL-101(Fe) with a uniform size distribution was successfully synthesized.

Figure 2B–E shows that all the activated samples had the same morphology—cubo-octahedral, which was same as that of M-0. However, the surface roughness of the particles showed some changes with the vacuum thermal activation. As shown in Figure 2A, the as-prepared MIL-101(Fe) had a dense and smooth surface. In contrast, the surfaces of M-120 and M-150 were less dense, and it was even rough and loose for M-200. The change in the particle texture from dense to loose was also observed in TEM (Supplementary Materials Figures S1–S4). This may be due to the removal of free or bond water molecules from the framework of MIL-101(Fe).

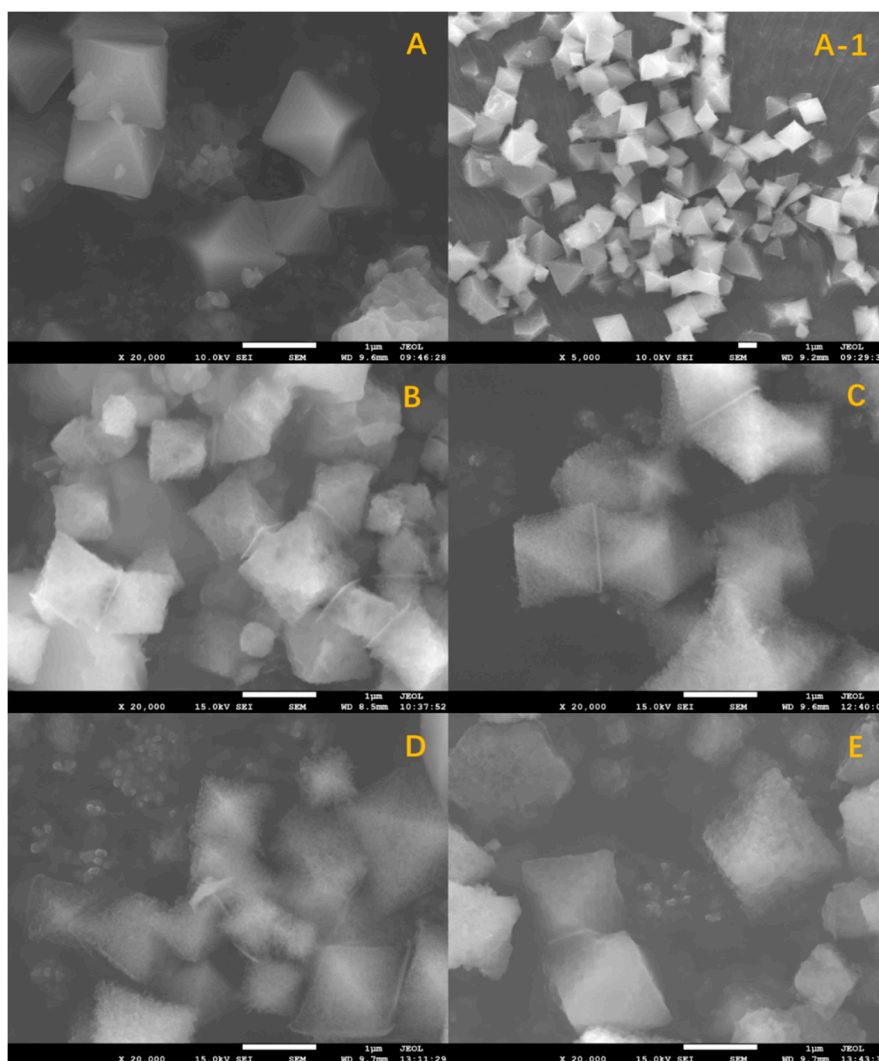


Figure 2. SEM micrographs of as-prepared MIL-101(Fe) and activated samples. (A) M-0, at magnifications of 20,000 \times ; (A-1): M-0, at magnifications of 5000 \times ; (B) M-120, at magnifications of 20,000 \times ; (C) M-150, at magnifications of 20,000 \times ; (D) M-170, at magnifications of 20,000 \times ; (E) M-200, at magnifications of 20,000 \times .

2.2. Catalytic Performance

The catalytic performances of as-prepared MIL-101(Fe) and activated samples were investigated through X-3B removal experiments. As shown in Figure 3, no appreciable X-3B removal was observed when persulfate (PS) was applied alone. When prepared samples were introduced into the system, sharp increases in the removal ratio of X-3B were subsequently observed, which demonstrated that all the samples were potential catalysts for PS activation.

It can obviously be seen that the removal ratios of X-3B over M-120/150/170/200 were much higher than that of M-0. After a 180 min reaction, the X-3B removal ratio reached 90.3%, 95.7%, 95.2%, and 92.5% for M-120, M-150, M-170, and M-200, respectively. The X-3B removal ratio was just 67.3% for M-0. This implies that vacuum thermal activation did have an influence on the catalytic capacity of MIL-101(Fe).

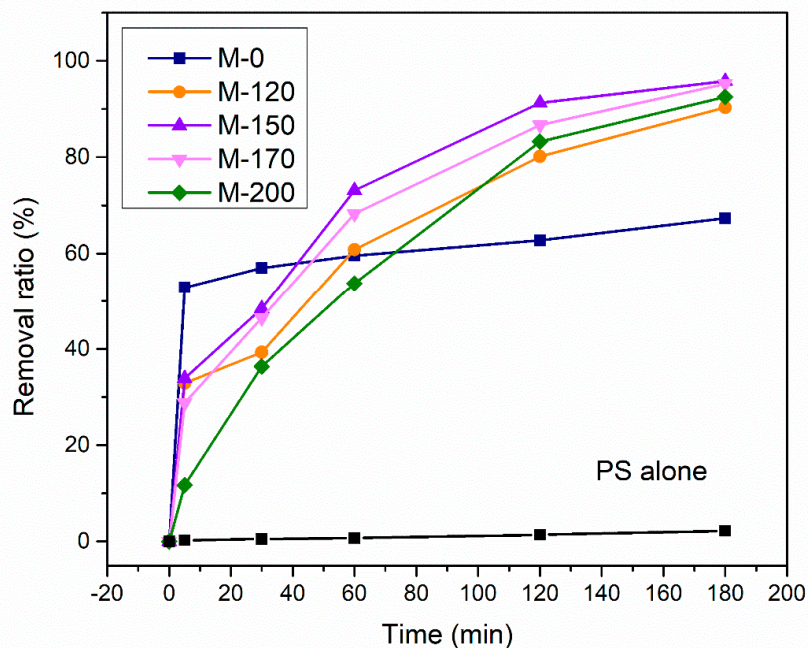


Figure 3. Removal of X-3B under different processes. Experimental conditions: (X-3B) = 100 mg L⁻¹, (PS) = 15 mmol L⁻¹, catalyst dosage = 0.1 g L⁻¹, T = 25 °C.

It is worth noting that the adsorption of X-3B by M-0/120/150/170/200 also contributes to the removal of X-3B (Figure 4). For a visual comparison of the catalytic ability of all samples, the value of the removal ratio was processed by subtracting the part caused by adsorption. As depicted in Figure 5, the removal ratio increased with the increase in activation temperature. It was proven that a higher temperature of vacuum thermal activation caused a higher catalytic capacity of MIL-101(Fe). This may be attributed to the change in the mixed-valence state of iron in MIL-101(Fe) which played a key role in PS activation.

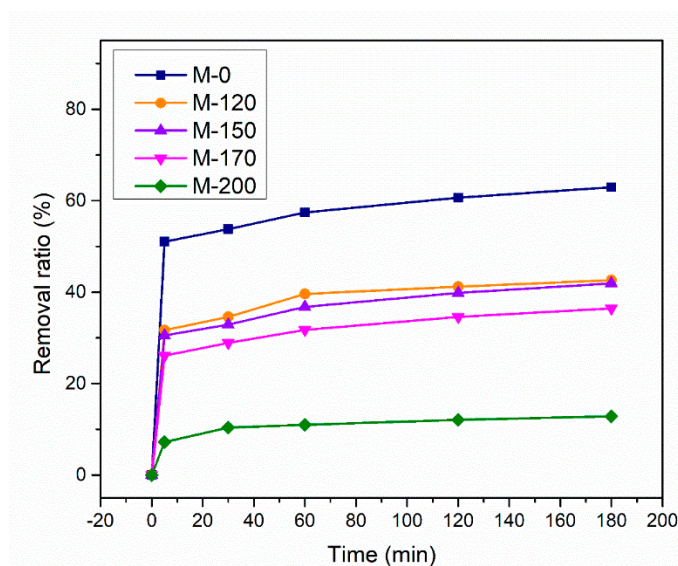


Figure 4. The X-3B adsorption of all samples. Experimental conditions: (X-3B) = 100 mg L⁻¹, (PS) = 15 mmol L⁻¹, catalyst dosage = 0.1 g L⁻¹, T = 25 °C.

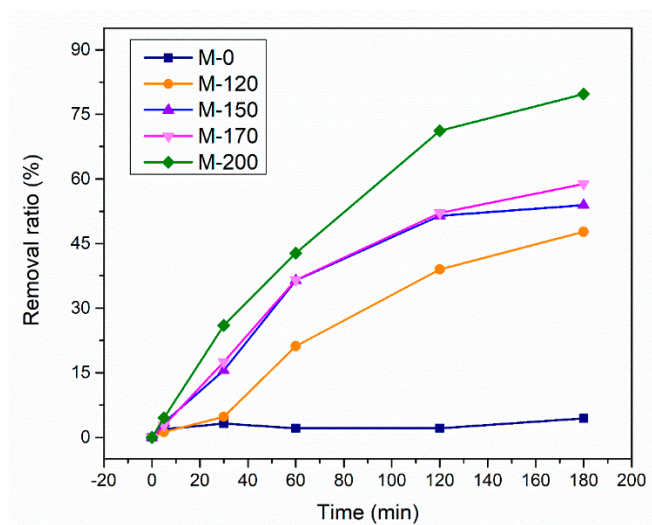


Figure 5. Catalytic performance of all samples (subtract the value of adsorption). Experimental conditions: (X-3B) = 100 mg L⁻¹, (PS) = 15 mmol L⁻¹, catalyst dosage = 0.1 g L⁻¹, T = 25 °C.

2.3. Mechanism

2.3.1. Mixed-Valence State of Iron in MIL-101(Fe)

In order to verify the change in the mixed-valence state of iron in MIL-101(Fe) after the vacuum thermal activation, X-ray photoelectron spectroscopy (XPS) was used to analyze the chemical states of the Fe element. X-ray photoelectron spectroscopy is often used to study the composition of mixed-valence iron oxides, as it is extremely sensitive to Fe²⁺ and Fe³⁺. As shown in Figures 5 and 6, the Fe2p high-resolution spectra of all samples consisted of two main peaks at binding energies of 711.4 ± 0.3 and 724.8 ± 0.3 eV, which were assigned to Fe 2p_{3/2} and Fe 2p_{1/2}, respectively.

The Fe2p spectra were fitted into three components, corresponding to FeII (green), FeIII (orange), and satellite peaks (gray), as illustrated in Figures 6 and 7. The full width at half-maximum (FWHM) of FeII (or FeIII) peak in Fe 2p_{3/2} was consistent with the one in Fe 2p_{1/2}. Meanwhile, the ratio of the peak area of FeII (or FeIII) peak in Fe 2p_{3/2} and Fe 2p_{1/2} should keep to 2:1. The peak parameters are presented in Table 1.

As can be seen from Table 1, the relative content ratios of FeII/FeIII (calculated by peak area) of the activated samples were higher than that of as-prepared MIL-101(Fe). Furthermore, the ratios of FeII/FeIII increased with the increase of activation temperature. The ratio of FeII/FeIII of M-150 was very close to that of M-170, which was in accordance with the catalytic performance of these two samples (see Figure 5). This implies that vacuum thermal activation did have an influence on the chemical state of the iron center in MIL-101(Fe) and that a higher temperature was beneficial to promote the generation of FeII sites. In addition, an increase in the proportion of FeII could accelerate the decomposition of PS, for the activation capacity of FeII was higher than that of FeIII. The experimental results of the X-3B removal were consistent with the above statement.

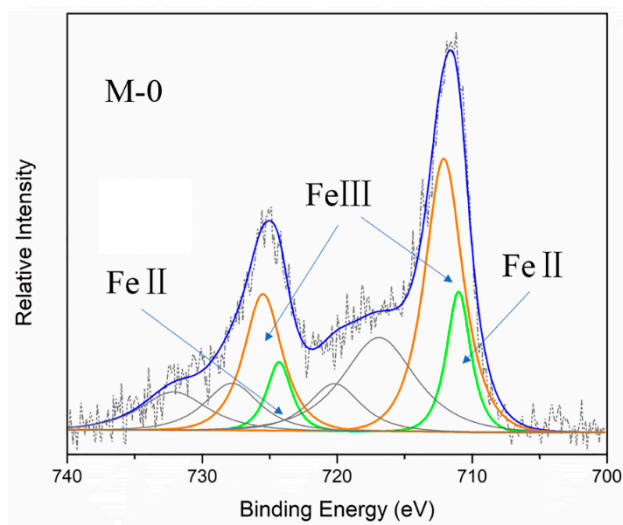


Figure 6. Fe2p high-resolution spectra of as-prepared MIL-101(Fe).

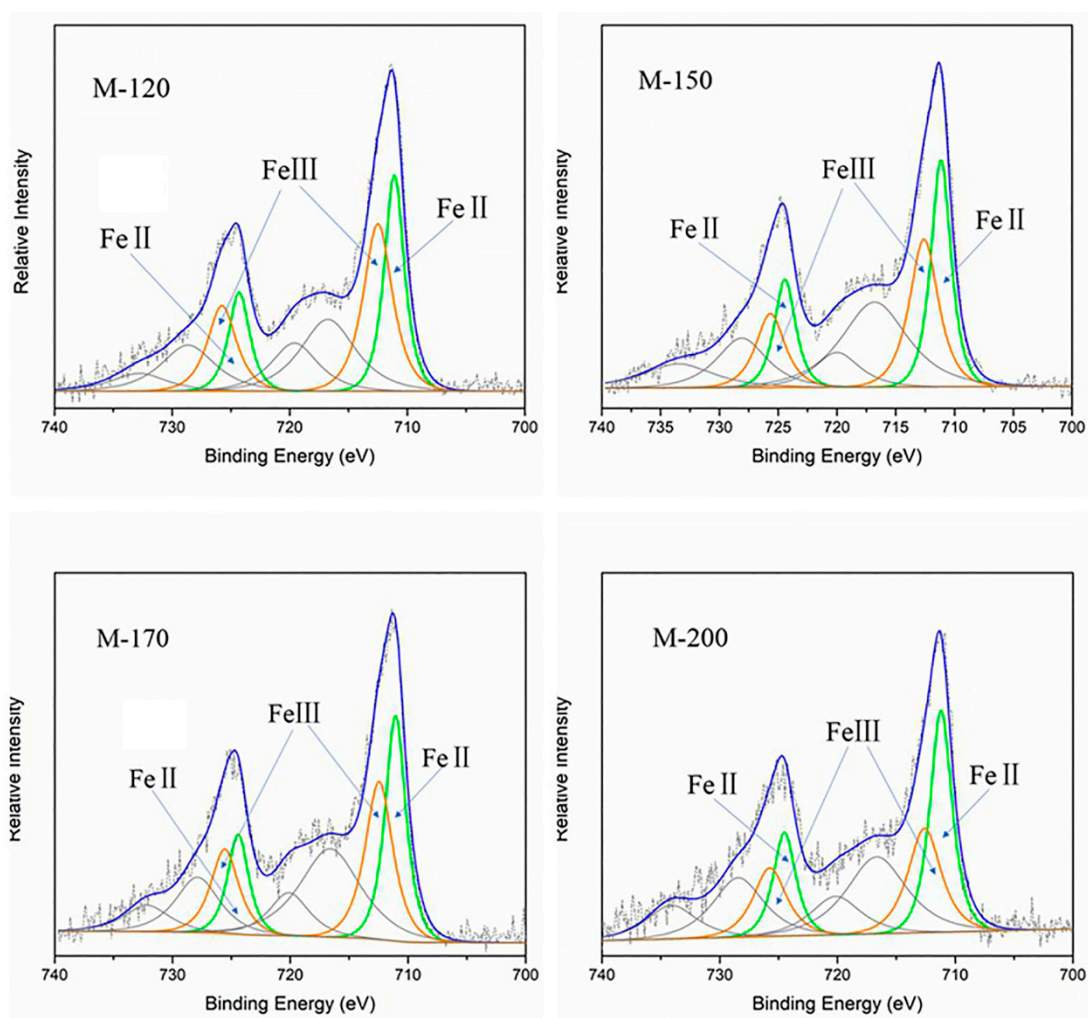


Figure 7. Fe2p high-resolution spectra of activated samples.

Table 1. Chemical states of Fe elements and the corresponding parameters.

Samples	Assignment	Peak Position	FWHM	FeII/FeIII	
M-0	Fe 2p _{3/2}	FeII	710.99	2.1	0.327
		FeIII	712.09	3.3	
	Fe 2p _{1/2}	FeII	724.29	2.15	
		FeIII	725.49	3.3	
M-120	Fe 2p _{3/2}	FeII	711.09	2.0	0.890
		FeIII	712.49	2.9	
	Fe 2p _{1/2}	FeII	724.29	2.1	
		FeIII	725.75	2.9	
M-150	Fe 2p _{3/2}	FeII	711.15	2.0	1.064
		FeIII	712.60	2.89	
	Fe 2p _{1/2}	FeII	724.34	2.15	
		FeIII	725.66	2.89	
M-170	Fe 2p _{3/2}	FeII	711.05	2.08	1.070
		FeIII	712.45	2.78	
	Fe 2p _{1/2}	FeII	724.42	2.1	
		FeIII	725.55	2.8	
M-200	Fe 2p _{3/2}	FeII	711.19	2.2	1.417
		FeIII	712.59	3.3	
	Fe 2p _{1/2}	FeII	724.49	2.25	
		FeIII	725.73	3.3	

2.3.2. Quenching Experiments and EPR (Electron Paramagnetic Resonance) Tests

To identify the reactive species generated in an MIL-101(Fe)/PS system, quenching experiments were conducted with M-150. As is well known, methanol and tertiary butyl alcohol (TBA) are commonly used quenching agents, and methanol is regarded as a scavenger of both $\text{SO}_4^{\cdot-}$ and $\text{OH}\cdot$, while TBA is considered as a scavenger of only $\text{OH}\cdot$ rather than $\text{SO}_4^{\cdot-}$ [30]. Figure 8 displays the reduction in X-3B removal in the presence of different trapping agents.

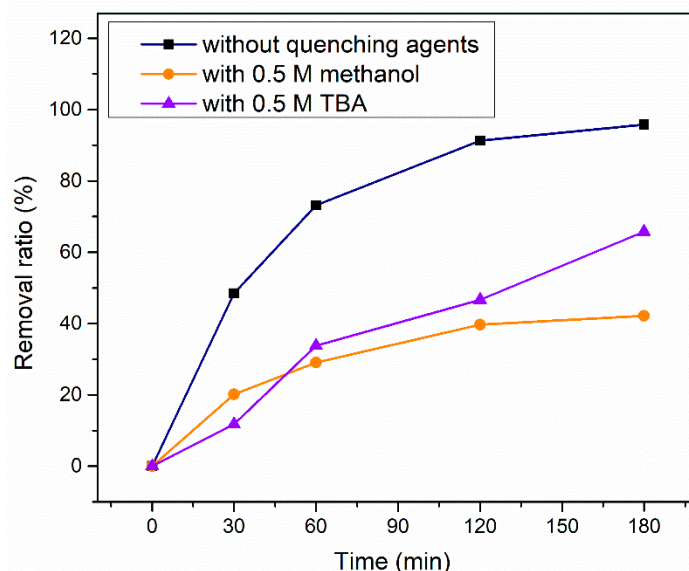


Figure 8. Influence of radical scavenger (methanol/TBA) on X-3B removal. Experimental conditions: (X-3B) = 100 mg L⁻¹, (PS) = 15 mmol L⁻¹, M-150 dosage = 0.1 g L⁻¹, T = 25 °C.

It can be found that the introduction of methanol caused the removal ratio of X-3B to decrease from 95.7% to 42.2% after 180 min. While the addition of TBA had a relatively moderate impact on the removal ratio. This indicated that both $\text{SO}_4^{\cdot-}$ and $\text{OH}\cdot$ were involved in the process of X-3B removal.

In order to gain insight into the predominant free radicals, electron paramagnetic resonance (EPR) studies were also conducted. As shown in Figure 9, the typical six-line patterns can be recognized as the signal of the $\text{DMPO-SO}_4^{\cdot-}$ adduct based on their hyperfine splitting constants ($\alpha_{\text{N}} = 13.01$ G, $\alpha_{\beta\text{-H}} = 10.22$ G, $\alpha_{\gamma 1\text{-H}} = 1.43$ G, $\alpha_{\gamma 2\text{-H}} = 0.79$ G), and the four split lines can be recognized as the signal of the $\text{DMPO-OH}\cdot$ adduct, according to their hyperfine splitting constants ($\alpha_{\beta\text{-H}} = 14.95$ G, $\alpha_{\text{N}} = 14.96$) [41,42].

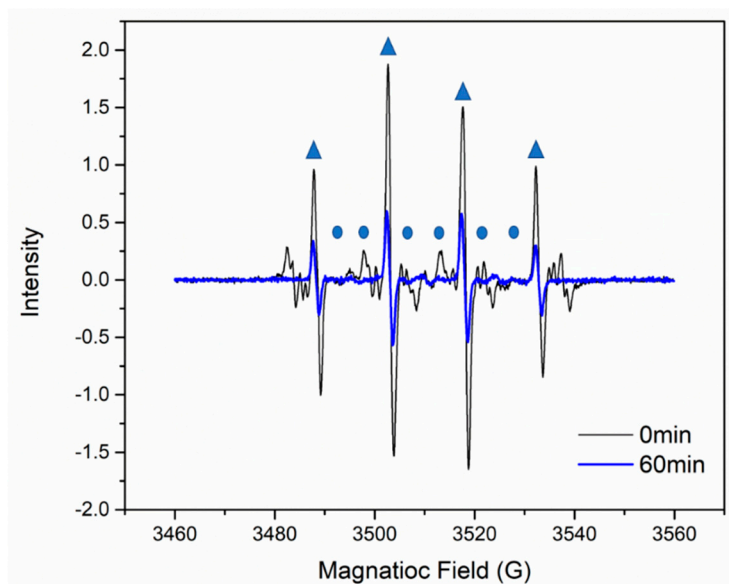


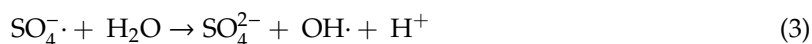
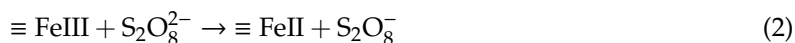
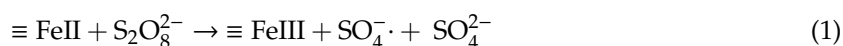
Figure 9. The electron paramagnetic resonance (EPR) spectra of the PS/M-150 system with DMPO (5, 5-Dimethyl-1-pyrroline-N-oxide) as a trapping agent. ▲ $\text{DMPO-OH}\cdot$ adduct; ● $\text{DMPO-SO}_4^{\cdot-}$ adduct; Experimental conditions: (PS) = 15 mmol L⁻¹, M-150 dosage = 0.1 g L⁻¹, (DMPO) = 0.9 mol L⁻¹, (X-3B) = 100 mg L⁻¹, T = 25 °C.

In addition, comparing the EPR spectra tested at the beginning of the reaction without X-3B (0 min, black line) and the one tested after the reaction had proceeded for 60 min (60 min, blue line), the intensity of the signals sharply decreased but did not disappear. This demonstrated that both $\text{SO}_4^{\cdot-}$ and $\text{OH}\cdot$ were continually generated in the PS/MIL-101(Fe) system for a long time. Meanwhile, both $\text{SO}_4^{\cdot-}$ and $\text{OH}\cdot$ contributed to the removal of X-3B.

2.3.3. Mechanism of Activation of PS by MIL-101(Fe)

It is evident that $\text{SO}_4^{\cdot-}$ and $\text{OH}\cdot$ are the key active species for removal of X-3B in a PS/MIL-101(Fe) system based on the results of the quenching experiments and EPR tests. It is noted that the relative content ratio of FeII/FeIII increased with the increase in the activation temperature which improved the catalytic performance of MIL-101(Fe). Thus, the activation mechanism is hypothesized as follows: First, the crystalline open structures of MIL-101(Fe) provided efficient entrances for penetration of reactant molecules. Second, the active iron sites, which distributed uniformly in the whole structure, were accessible for PS in the solution. Thus, the FeII sites could activate PS to generate $\text{SO}_4^{\cdot-}$ through a one-electron transition reaction, and the FeII sites changed into a trivalent state (Equation (1)). Meanwhile, the FeIII sites were also able to initiate the decomposition of PS and transformed into FeII sites with the generated $\text{S}_2\text{O}_8^{\cdot-}$ (Equation (2)) [43]. As active metal sites, FeII sites and FeIII sites converted into each other continuously with the activation of PS. Simultaneously, $\text{SO}_4^{\cdot-}$ could directly convert into $\text{OH}\cdot$ via hydrolysis reaction with water (at all pH conditions) (Equation (3)), and this

could explain the existence of $\text{OH}\cdot$ in this system (the solution pH was acidic). Besides, $\text{SO}_4^{\cdot-}$ and $\text{OH}\cdot$ could react with persulfate anions to generate additional $\text{S}_2\text{O}_8^{\cdot-}$ (Equations (4) and (5)).



2.4. Stability and Reusability

The reusability and stability are a prerequisite for the catalyst to be used in practical applications and, therefore, the activity of M-150 was assessed in five repeated X-3B removal experiments under the identical experimental conditions. After each run, catalyst was collected by centrifugation and washed with deionized water several times and then vacuum dried at 60 °C for 12 h which was the drying condition for as-prepared MIL-101(Fe). Several parallel experiments were carried out simultaneously to ensure the amount of catalyst was sufficient for each run. The results obtained with M-150 are shown in Figure 10. After a reaction of 180 min, the final X-3B removal ratio in the M-150/PS system was maintained above 90% for the first four recycling experiments and decreased to 87% for the 5th.

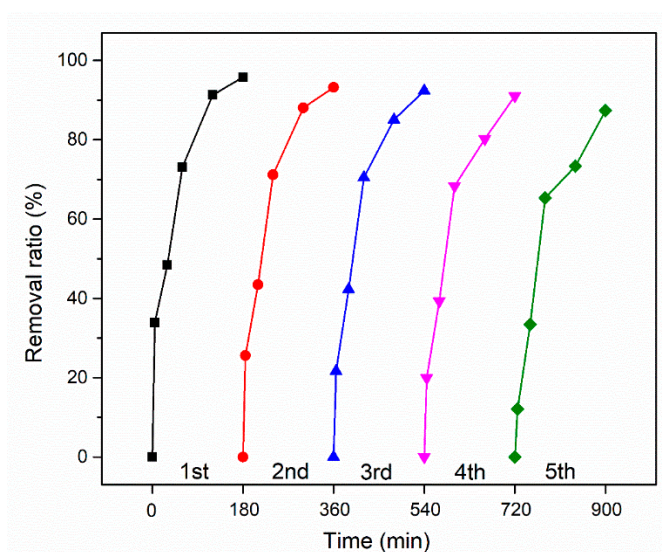


Figure 10. Reusability of M-150 for X-3B removal. Experimental conditions: (X-3B) = 100 mg L⁻¹, (PS) = 15 mmol L⁻¹, M-150 dosage = 0.1 g L⁻¹, T = 25 °C.

The surface morphology and crystal structure of M-150 after five recycling experiments were examined by SEM and XRD. As seen in Figure 11, the position of the diffraction peaks was very similar to that of pristine M-150, while the relative intensity of peaks had changed. This implies that, the used M-150 was still composed of crystalline particles, while there was some change in the structure of these particles. As depicted in Figure 12, an obvious distinction was observed between the as-prepared and the used M-150. The raw catalyst M-150 was composed of cubo-octahedron crystals with a uniform size distribution, whereas the image of the used catalyst shows rod-like particles and large particles with irregular shape. Therefore, the reduction of the X-3B removal ratio can be explained by the following reasons: a) the active metal sites of MIL-101(Fe) were occupied by adsorbed X-3B and the degradation intermediates; b) the change in the open structure of MIL-101(Fe) may have decreased the accessibility of the active iron sites for reactant molecules.

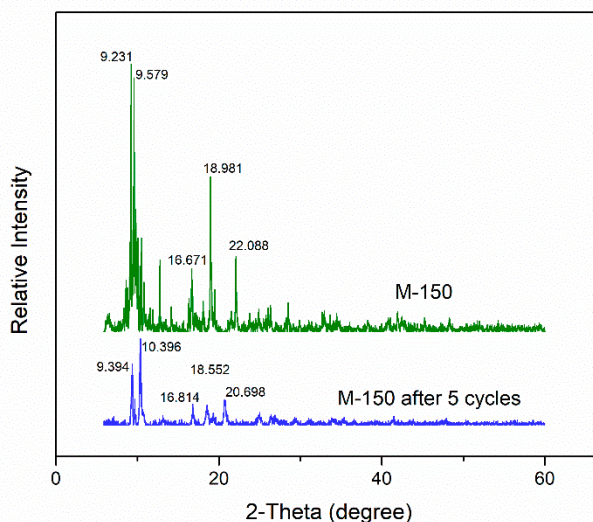


Figure 11. XRD patterns of M-150 before and after the recycling experiments.

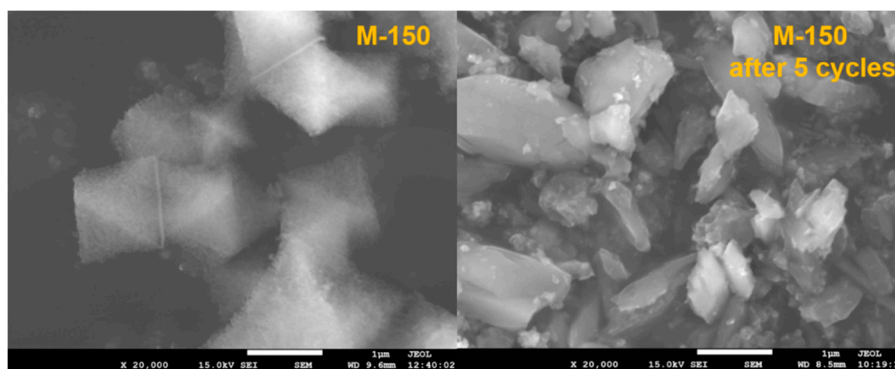


Figure 12. SEM micrographs of M-150 before and after the recycling experiments.

These results demonstrate that M-150, without regeneration, could effectively activate PS to remove X-3B for at least 5 runs and approximately 900 min.

3. Materials and Methods

3.1. Chemical Reagents

Iron chloride hexahydrate ($\text{FeCl}_3 \cdot 6\text{H}_2\text{O}$) was purchased from DaMao Chemical Co. (Tianjin, China). Terephthalic acid (PTA) and tert-butyl alcohol (TBA) were purchased from Aladdin Co. (Shanghai, China). *N,N*-Dimethylformamide (DMF) was purchased from SiYou Chemical Co. (Tianjin, China). Ethanol and methanol were purchased from BeiChenFangZheng Chemical Co. (Tianjin, China). The commercially available dye X-3B was supplied by JiangLai Biological Co. (Shanghai, China). Potassium persulfate (PS) was purchased from TianLi Chemical Co. (Tianjin, China). 5,5-Dimethyl-1-pyrroline-*N*-oxide (DMPO) was purchased from APExBIO Technology LLC (Shanghai, China).

All reagents were of analytical reagent grade or higher and used without further purification. All aqueous solutions were made using reverse-osmosis-type quality water (conductivity $< 1 \mu\text{S cm}^{-1}$).

3.2. Preparation and Characterization of Catalysts

The MIL-101(Fe) was prepared as described in the literature [44,45] with some minor modifications. In brief, a mixture of 0.675 g of $\text{FeCl}_3 \cdot 6\text{H}_2\text{O}$, 0.206 g PTA, and 15 mL DMF was heated at 110°C for 20 h in a Teflon-lined stainless-steel bomb. The resulting dark red solid was collected via centrifugation,

washed 3 times with DMF and twice with hot ethanol (60 °C, 3 h), and finally dried in a vacuum oven (60 °C, 12 h).

Then, the synthesized MIL-101(Fe) was divided into 5 parts, one was denoted as M-0 without further treatment, the other four were treated, respectively, in a vacuum oven at a required temperature (120 °C, 150 °C, 170 °C, and 200 °C) for 7 h and denoted as M-120, M-150, M-170, and M-200, respectively. The resulting powder samples were kept in a desiccator containing allochroic silica gel at room temperature until needed.

The X-ray diffraction (XRD) patterns of the samples were obtained on a D8-ADVANCE-A25 power diffractometer (Bruker, Germany) using Cu-K α radiation ($\lambda = 1.5418 \text{ \AA}$) in the range of 5–70° with a step size of 0.02°. The surface morphology of the samples was observed using a JSM-7001F (JEOL, Japan) scanning electron microscope (SEM). The X-ray photoelectron spectroscopy (XPS) of the samples was recorded on an AXIS ULTRA DLD using an Al-K α X-ray source (1486.6 eV).

3.3. Catalytic and Adsorption Experiments

Typical catalytic experiments were carried out in 250 ml conical flasks containing 100 mL of X-3B solution at 25 °C without pH adjustment. The flasks were shaken at the speed of 180 rpm for 180 min in a constant temperature shaker. Unless otherwise specified, all experiments were performed at initial concentration of 100 mg L⁻¹ of X-3B and 15 mmol L⁻¹ of PS and 0.1 g L⁻¹ of catalyst. A control experiment with PS alone was also carried out. The conditions of the adsorption experiments were the same as the catalytic experiments only without the addition of PS.

At given time intervals, a certain amount of solution was sampled and filtered through a 0.22 μm Millipore membrane and then analyzed at 540.0 nm (maximum absorbance wavelength of X-3B) with a UV-5200 UV/VIS spectrophotometer (Metash, Shanghai).

3.4. EPR Tests

Electron paramagnetic resonance (EPR) experiments were conducted by mixing 100 μl of reaction solution with 10 μl DMPO in a 1 mL sample vial and then tested and recorded immediately. The EPR spectra were recorded at liquid nitrogen temperature on an EMXPLUS10/12 spectrometer (Bruker, Germany) with the conditions as follows: magnetic field: center field = 3510.00 G, sweep width = 100.0 G, sweep time = 60.00 s, sample g-factor = 2.0000; signal channel: receiver gain = 30 dB, mod. amp = 0.600 G; microwave: attenuation = 13.0 dB, power = 10.02 mW.

4. Conclusions

In this study, vacuum thermal activation was used to activate MIL-101(Fe) for the first time. The as-prepared MIL-101(Fe) and the samples activated at different temperatures of vacuum thermal activation were characterized by XRD, SEM, and XPS. Meanwhile, the catalytic capacity for PS activation was investigated through X-3B removal experiments. The results showed that the vacuum thermal activation did have positive impact on the catalytic capacity of MIL-101(Fe) with a negligible change in the crystal structure and particle morphology. It is worth noting that a higher temperature of vacuum thermal activation was beneficial to increase the amount of FeII sites, demonstrated by the increase in the relative content ratio of FeII/FeIII. With the increase in the ratio of FeII/FeIII from 0.327 (M-0) to 1.064 (M-150), the final removal ratio was increased to 95.78% in the M-150/PS system which was nearly 1.5 times as much as that in the M-0/PS system. In addition, quenching experiments and EPR tests showed that $\text{SO}_4^{\cdot-}$ and OH^{\cdot} were generated in the MIL-101(Fe)/PS system, and both of them contributed to the removal of X-3B. The stability and reusability of the activated sample were also evaluated by recycling experiments, and the results imply that M-150, without regeneration, could effectively activate PS to remove X-3B for at least 5 runs and approximately 900 min. This finding provides a new insight into the application of vacuum thermal activation for Fe-based metal-organic frameworks and highlights the great potential of MIL-101(Fe)/PS systems for the removal of azo dye.

Supplementary Materials: The following are available online at <http://www.mdpi.com/2073-4344/9/11/906/s1>, Figure S1: TEM image of M-0, Figure S2: TEM image of M-120, Figure S3: TEM image of M-170, Figure S4: TEM image of M-200.

Author Contributions: Conceptualization, J.Y.; Data curation, J.Y.; Funding acquisition, Z.Z., Z.H. and Y.C.; Investigation, J.Y.; Methodology, J.Y.; Project administration, Y.C.; Resources, Z.H.; Supervision, Z.Z. and Z.H.; Validation, Z.Z.; Visualization, J.Y.; Writing—original draft, J.Y.; Writing—review and editing, Z.Z.

Funding: This research was funded by the National Natural Science Foundation of China (21507140) and the Natural Science Foundation of Shanxi Province (201701D221232).

Conflicts of Interest: The authors declare no conflict of interest.

References

1. Neamtu, M.; Siminiceanu, I.; Yediler, A.; Kettrup, A. Kinetics of decolorization and mineralization of reactive azo dyes in aqueous solution by the UV/H₂O₂ oxidation. *Dye. Pigment.* **2002**, *53*, 93–99. [[CrossRef](#)]
2. Hu, C.; Hu, X.; Wang, L.; Qu, J.; Wang, A. Visible-light-induced photocatalytic degradation of azo dyes in aqueous AgI/TiO₂ dispersion. *Environ. Sci. Technol.* **2006**, *40*, 7903–7907. [[CrossRef](#)] [[PubMed](#)]
3. Vinodgopal, K.; Wynkoop, D.E.; Kamat, P.V. Environmental Photochemistry on Semiconductor Surfaces: Photosensitized Degradation of a Textile Azo Dye, Acid Orange 7, on TiO₂ Particles Using Visible Light. *Environ. Sci. Technol.* **1996**, *30*, 1660–1666. [[CrossRef](#)]
4. de Lima, R.O.A.; Bazo, A.P.; Salvadori, D.M.F.; Rech, C.M.; de Palma Oliveira, D.; de Aragão Umbuzeiro, G. Mutagenic and carcinogenic potential of a textile azo dye processing plant effluent that impacts a drinking water source. *Mutat. Res. Genet. Toxicol. Environ. Mutagen.* **2007**, *626*, 53–60. [[CrossRef](#)] [[PubMed](#)]
5. Cao, C.; Xiao, L.; Chen, C.; Shi, X.; Cao, Q.; Gao, L. In situ preparation of magnetic Fe₃O₄/chitosan nanoparticles via a novel reduction–precipitation method and their application in adsorption of reactive azo dye. *Powder Technol.* **2014**, *260*, 90–97. [[CrossRef](#)]
6. Hsueh, C.L.; Huang, Y.H.; Wang, C.C.; Chen, C.Y. Degradation of azo dyes using low iron concentration of Fenton and Fenton-like system. *Chemosphere* **2005**, *58*, 1409–1414. [[CrossRef](#)]
7. Peternel, I.; Kusic, H.; Marin, V.; Koprivanac, N. UV-assisted persulfate oxidation: The influence of cation type in the persulfate salt on the degradation kinetics of an azo dye pollutant. *React. Kinet. Mech. Catal.* **2013**, *108*, 17–39. [[CrossRef](#)]
8. Li, J.J.; Wu, L.; Liu, P.F.; Liu, L.J.; Zhang, B. Effect of Annealing Temperature of Fe₇₈Si₉B₁₃ Amorphous Ribbons for Activation of Persulfate on Azo Dye Degradation. *Adv. Funct. Mater.* **2018**, 285–292.
9. Ma, Y.H.; Chen, F.; Yang, Q.; Zhong, Y.; Shu, X.Y.; Yao, F.B.; Xie, T.; Li, X.M.; Wang, D.B.; Zeng, G.M. Sulfate radical induced degradation of Methyl Violet azo dye with CuFe layered doubled hydroxide as heterogeneous photoactivator of persulfate. *J. Environ. Manag.* **2018**, *227*, 406–414. [[CrossRef](#)]
10. Chen, J.B.; Hong, W.; Huang, T.Y.; Zhang, L.M.; Li, W.W.; Wang, Y. Activated carbon fiber for heterogeneous activation of persulfate: Implication for the decolorization of azo dye. *Environ. Sci. Pollut. Res.* **2016**, *23*, 18564–18574. [[CrossRef](#)]
11. Zhu, J.P.; Lin, Y.L.; Zhang, T.Y.; Cao, T.C.; Xu, B.; Pan, Y.; Zhang, X.T.; Gao, N.Y. Modelling of iohexol degradation in a Fe(II)-activated persulfate system. *Chem. Eng. J.* **2019**, *367*, 86–93. [[CrossRef](#)]
12. Ling, L.; Li, Z.B.; Fang, J.Y.; Shang, C. Control of bromate formation in UV/peroxymonosulfate, UV/persulfate and Co/peroxymonosulfate processes by ammonia, chlorine-ammonia, and ammonia-chlorine processes. *Abstr. Papers Am. Chem. Soc.* **2015**, *250*, 26.
13. Felix-Navarro, R.M.; Lin, S.W.; Zizumbo-Lopez, A.; Perez-Sicairos, S.; Reynoso-Soto, E.A.; Espinoza-Gomez, J.H. 1,4-Dioxane Degradation Using Persulfate Ion and Ag(I) Ion. *J. Mex. Chem. Soc.* **2013**, *57*, 127–132. [[CrossRef](#)]
14. Wang, J.-L.; Wang, C.; Lin, W. Metal–Organic Frameworks for Light Harvesting and Photocatalysis. *ACS Catal.* **2012**, *2*, 2630–2640. [[CrossRef](#)]
15. Li, D.; Chen, D.; Yao, Y.; Lin, J.; Gong, F.; Wang, L.; Luo, L.; Huang, Z.; Zhang, L. Strong enhancement of dye removal through addition of sulfite to persulfate activated by a supported ferric citrate catalyst. *Chem. Eng. J.* **2016**, *288*, 806–812. [[CrossRef](#)]

16. Zou, J.; Ma, J.; Chen, L.; Li, X.; Guan, Y.; Xie, P.; Pan, C. Rapid Acceleration of Ferrous Iron/Peroxymonosulfate Oxidation of Organic Pollutants by Promoting Fe(III)/Fe(II) Cycle with Hydroxylamine. *Environ. Sci. Technol.* **2013**, *47*, 11685–11691. [[CrossRef](#)]
17. Sun, L.; Yao, Y.; Wang, L.; Mao, Y.; Huang, Z.; Yao, D.; Lu, W.; Chen, W. Efficient removal of dyes using activated carbon fibers coupled with 8-hydroxyquinoline ferric as a reusable Fenton-like catalyst. *Chem. Eng. J.* **2014**, *240*, 413–419. [[CrossRef](#)]
18. Weng, C.-H.; Tao, H. Highly efficient persulfate oxidation process activated with Fe⁰ aggregate for decolorization of reactive azo dye Remazol Golden Yellow. *Arab. J. Chem.* **2018**, *11*, 1292–1300. [[CrossRef](#)]
19. Matzek, L.W.; Carter, K.E. Activated persulfate for organic chemical degradation: A review. *Chemosphere* **2016**, *151*, 178–188. [[CrossRef](#)]
20. Ahn, Y.-Y.; Bae, H.; Kim, H.-I.; Kim, S.-H.; Kim, J.-H.; Lee, S.-G.; Lee, J. Surface-loaded metal nanoparticles for peroxymonosulfate activation: Efficiency and mechanism reconnaissance. *Appl. Catal. B Environ.* **2019**, *241*, 561–569. [[CrossRef](#)]
21. Yan, J.; Han, L.; Gao, W.; Xue, S.; Chen, M. Biochar supported nanoscale zerovalent iron composite used as persulfate activator for removing trichloroethylene. *Bioresour. Technol.* **2015**, *175*, 269–274. [[CrossRef](#)] [[PubMed](#)]
22. Shi, Q.; Li, A.; Qing, Z.; Li, Y. Oxidative degradation of Orange G by persulfate activated with iron-immobilized resin chars. *J. Ind. Eng. Chem.* **2015**, *25*, 308–313. [[CrossRef](#)]
23. Maksimchuk, N.V.; Zalomaeva, O.V.; Skobelev, I.Y.; Kovalenko, K.A.; Fedin, V.P.; Kholdeeva, O.A. Metal-organic frameworks of the MIL-101 family as heterogeneous single-site catalysts. *Proc. R. Soc. A Math. Phys. Eng. Sci.* **2012**, *468*, 2017–2034. [[CrossRef](#)]
24. Wang, D.; Huang, R.; Liu, W.; Sun, D.; Li, Z. Fe-Based MOFs for Photocatalytic CO₂ Reduction: Role of Coordination Unsaturated Sites and Dual Excitation Pathways. *ACS Catal.* **2014**, *4*, 4254–4260. [[CrossRef](#)]
25. Wang, D.; Jia, F.; Wang, H.; Chen, F.; Fang, Y.; Dong, W.; Zeng, G.; Li, X.; Yang, Q.; Yuan, X. Simultaneously efficient adsorption and photocatalytic degradation of tetracycline by Fe-based MOFs. *J. Colloid Interface Sci.* **2018**, *519*, 273–284. [[CrossRef](#)]
26. Férey, G.; Mellot-Draznieks, C.; Serre, C.; Millange, F. Crystallized Frameworks with Giant Pores: Are There Limits to the Possible? *Acc. Chem. Res.* **2005**, *38*, 217–225. [[CrossRef](#)]
27. Gao, Y.W.; Li, S.M.; Li, Y.X.; Yao, L.Y.; Zhang, H. Accelerated photocatalytic degradation of organic pollutant over metal-organic framework MIL-53(Fe) under visible LED light mediated by persulfate. *Appl. Catal. B Environ.* **2017**, *202*, 165–174. [[CrossRef](#)]
28. Wang, J.M.; Wan, J.Q.; Ma, Y.W.; Wang, Y.; Pu, M.J.; Guan, Z.Y. Metal-organic frameworks MIL-88A with suitable synthesis conditions and optimal dosage for effective catalytic degradation of Orange G through persulfate activation. *RSC Adv.* **2016**, *6*, 112502–112511. [[CrossRef](#)]
29. Li, X.H.; Guo, W.L.; Liu, Z.H.; Wang, R.Q.; Liu, H. Fe-based MOFs for efficient adsorption and degradation of acid orange 7 in aqueous solution via persulfate activation. *Appl. Surf. Sci.* **2016**, *369*, 130–136. [[CrossRef](#)]
30. Yue, X.X.; Guo, W.L.; Li, X.H.; Zhou, H.H.; Wang, R.Q. Core-shell Fe₃O₄@MIL-101(Fe) composites as heterogeneous catalysts of persulfate activation for the removal of Acid Orange 7. *Environ. Sci. Pollut. Res.* **2016**, *23*, 15218–15226. [[CrossRef](#)]
31. Zhang, M.W.; Yang, M.T.; Tong, S.P.; Lin, K.Y.A. Ferrocene-modified iron-based metal-organic frameworks as an enhanced catalyst for activating oxone to degrade pollutants in water. *Chemosphere* **2018**, *213*, 295–304. [[CrossRef](#)] [[PubMed](#)]
32. Wang, Y.; Guo, W.L.; Li, X.H. Activation of persulfates by ferrocene-MIL-101(Fe) heterogeneous catalyst for degradation of bisphenol A. *RSC Adv.* **2018**, *8*, 36477–36483. [[CrossRef](#)]
33. Gong, Y.; Yang, B.; Zhang, H.; Zhao, X. A g-C₃N₄/MIL-101(Fe) heterostructure composite for highly efficient BPA degradation with persulfate under visible light irradiation. *J. Mater. Chem. A* **2018**, *6*, 23703–23711. [[CrossRef](#)]
34. Wuttke, S.; Bazin, P.; Vimont, A.; Serre, C.; Seo, Y.-K.; Hwang, Y.K.; Chang, J.-S.; Férey, G.; Daturi, M. Discovering the Active Sites for C₃ Separation in MIL-100(Fe) by Using Operando IR Spectroscopy. *Chem. Eur. J.* **2012**, *18*, 11959–11967. [[CrossRef](#)]
35. Aggarwal, H.; Bhatt, P.M.; Bezuidenhout, C.X.; Barbour, L.J. Direct Evidence for Single-Crystal to Single-Crystal Switching of Degree of Interpenetration in a Metal–Organic Framework. *J. Am. Chem. Soc.* **2014**, *136*, 3776–3779. [[CrossRef](#)]

36. Yoon, J.W.; Seo, Y.-K.; Hwang, Y.K.; Chang, J.-S.; Leclerc, H.; Wuttke, S.; Bazin, P.; Vimont, A.; Daturi, M.; Bloch, E.; et al. Controlled Reducibility of a Metal–Organic Framework with Coordinatively Unsaturated Sites for Preferential Gas Sorption. *Angew. Chem. Int. Ed.* **2010**, *49*, 5949–5952. [[CrossRef](#)]
37. Kholdeeva, O.A.; Skobelev, I.Y.; Ivanchikova, I.D.; Kovalenko, K.A.; Fedin, V.P.; Sorokin, A.B. Hydrocarbon oxidation over Fe- and Cr-containing metal-organic frameworks MIL-100 and MIL-101-a comparative study. *Catal. Today* **2014**, *238*, 54–61. [[CrossRef](#)]
38. Xie, Q.; Li, Y.; Lv, Z.; Zhou, H.; Yang, X.; Chen, J.; Guo, H. Effective Adsorption and Removal of Phosphate from Aqueous Solutions and Eutrophic Water by Fe-based MOFs of MIL-101. *Sci. Rep.* **2017**, *7*, 3316. [[CrossRef](#)]
39. Skobelev, I.Y.; Sorokin, A.B.; Kovalenko, K.A.; Fedin, V.P.; Kholdeeva, O.A. Solvent-free allylic oxidation of alkenes with O₂ mediated by Fe- and Cr-MIL-101. *J. Catal.* **2013**, *298*, 61–69. [[CrossRef](#)]
40. Lebedev, O.I.; Millange, F.; Serre, C.; van Tendeloo, G.; Férey, G. First Direct Imaging of Giant Pores of the Metal–Organic Framework MIL-101. *Chem. Mater.* **2005**, *17*, 6525–6527. [[CrossRef](#)]
41. Pu, M.J.; Ma, Y.W.; Wan, J.Q.; Wang, Y.; Wang, J.M.; Brusseau, M.L. Activation performance and mechanism of a novel heterogeneous persulfate catalyst: Metal-organic framework MIL-53(Fe) with Fe-II/Fe-III mixed-valence coordinatively unsaturated iron center. *Catal. Sci. Technol.* **2017**, *7*, 1129–1140. [[CrossRef](#)] [[PubMed](#)]
42. Liu, C.; Wang, Y.P.; Zhang, Y.T.; Li, R.Y.; Meng, W.D.; Song, Z.L.; Qi, F.; Xu, B.B.; Chu, W.; Yuan, D.H.; et al. Enhancement of Fe@porous carbon to be an efficient mediator for peroxy monosulfate activation for oxidation of organic contaminants: Incorporation NH₂-group into structure of its MOF precursor. *Chem. Eng. J.* **2018**, *354*, 835–848. [[CrossRef](#)]
43. Joo, S.H. Advanced Treatment of Reverse Osmosis Concentrate by Integrated Activated Carbon and Iron-Activated Persulfate Oxidation. *Water Air Soil Pollut.* **2014**, *225*, 2076. [[CrossRef](#)]
44. Ortiz-Gomez, I.; Salinas-Castillo, A.; Garcia, A.G.; Alvarez-Bermejo, J.A.; de Orbe-Paya, I.; Rodriguez-Dieguez, A.; Capitan-Vallvey, L.F. Microfluidic paper-based device for colorimetric determination of glucose based on a metal-organic framework acting as peroxidase mimetic. *Microchim. Acta* **2018**, *185*, 47. [[CrossRef](#)] [[PubMed](#)]
45. Taylor-Pashow, K.M.L.; della Rocca, J.; Xie, Z.; Tran, S.; Lin, W. Postsynthetic Modifications of Iron-Carboxylate Nanoscale Metal–Organic Frameworks for Imaging and Drug Delivery. *J. Am. Chem. Soc.* **2009**, *131*, 14261–14263. [[CrossRef](#)] [[PubMed](#)]



© 2019 by the authors. Licensee MDPI, Basel, Switzerland. This article is an open access article distributed under the terms and conditions of the Creative Commons Attribution (CC BY) license (<http://creativecommons.org/licenses/by/4.0/>).